



1

2 **Remote sensing and modeling analysis of the extreme dust storm hitting**  
3 **Middle East and Eastern Mediterranean in September 2015**

4

5

6 **Solomos Stavros<sup>1</sup>, Albert Ansmann<sup>2</sup>, Rodanthi-Elisavet Mamouri<sup>3</sup>, Ioannis Biniotoglou<sup>1,5</sup>, Platon**  
7 **Patlakas<sup>4</sup>, Eleni Marinou<sup>1,6</sup> and Vassilis Amiridis<sup>1</sup>**

8

9 <sup>1</sup>Institute for Astronomy, Astrophysics, Space Applications and Remote Sensing (IAASARS), National  
10 Observatory of Athens, Athens, Greece

11 <sup>2</sup>Leibniz Institute for Tropospheric Research, Leipzig, Germany

12 <sup>3</sup>Cyprus University of Technology, Department of Civil Engineering and Geomatics, Limassol, Cyprus

13 <sup>4</sup>School of Physics, Division of Environment and Meteorology, University of Athens, Athens, Greece

14 <sup>5</sup>National Institute of R&D for Optoelectronics, Magurele, Ilfov, Romania

15 <sup>6</sup>Laboratory of Atmospheric Physics, Physics Department, Aristotle University of Thessaloniki, 54124,  
16 Thessaloniki, Greece

17

18 **Abstract** The extreme dust storm that affected Middle East and the Eastern Mediterranean in  
19 September 2015 resulted in record-breaking dust loads over Cyprus with aerosol optical depth  
20 exceeding 5.0 at 550 nm. We analyze this event using profiles from the European Aerosol Research  
21 Lidar Network (EARLINET), the Cloud-Aerosol Lidar and Infrared Pathfinder Satellite Observation  
22 (CALIPSO), geostationary observations from the Meteosat Second Generation - Spinning Enhanced  
23 Visible and Infrared Imager (MSG-SEVIRI) and high resolution simulations with the Regional  
24 Atmospheric Modeling System (RAMS). The analysis reveals the main mechanisms that resulted in  
25 the generation and persistence of the dust cloud over Middle-East and Cyprus. A combination of  
26 meteorological and surface processes is found: (a) the development of a thermal low at the area of  
27 Syria that results in unstable atmospheric conditions and dust mobilization at this area; (b) the  
28 convective activity over North Iraq that triggers the formation of a westward moving haboob that  
29 merges with the previously elevated dust layer; and (c) the changes in land use due to war at the  
30 areas of North Iraq and Syria that enhances dust erodibility.

31



## 32 1. Introduction

33

34 A record dust storm affected the entire Middle East and Cyprus in September 2015. Remote sensing  
35 observations and in-situ measurements of Arabian dust from this episode during 7-11 September  
36 2015 are presented by Mamouri et al. (2016) for the station of Limassol (34.7°N, 33°E). As reported  
37 in their article, the extreme amounts of dust over Middle East and East Mediterranean originate  
38 from the desert and arid areas of Syria and North Iraq. Triggered by this work, we analyze here the  
39 main processes that resulted in the mobilization of dust due to a combination of cyclonic flow and  
40 haboob formation.

41 Haboobs are local and mesoscale atmospheric density currents that mobilize huge amounts of dust  
42 and create a propagating dust wall extending up to 2-3 km in the troposphere (Knippertz et al.,  
43 2009; Solomos et al., 2012). These systems are well known by local populations at desert and arid  
44 areas worldwide due to their devastating impact in visibility and human health (e.g. Schepanski et  
45 al., 2009; Emmel et al., 2010). The responsible mechanism for haboob formation is the generation  
46 of a cold pool of ambient air due to evaporative cooling. The rain and ice condensates evaporate (or  
47 melt) as they fall through the warmer and unsaturated air and the absorption of latent heat from  
48 the phase changes leads in a vigor cooling of the surrounding air. When these convective outflow  
49 boundaries travel over bare soil and desert areas they result in the generation of a propagating dust  
50 wall. The scale of the processes that participate in the generation of such atmospheric density  
51 currents ranges from synoptic down to mesoscale and local. As a result, haboobs and their effects in  
52 weather and air-quality cannot be resolved by the coarse global model resolutions (Marsham et al.,  
53 2013). Moreover, haboobs usually generate over remote arid areas where no in-situ networks are  
54 present and inside dust-storm measurements can only be obtained during field campaign  
55 experiments (e.g. SAMUM 1 & 2, Ansmann et al., 2011; FENNEC, Ryder et al., 2015). Following these  
56 limitations, most of the efforts for the studying and forecasting of such intense dust episodes rely  
57 on passive and active remote sensing observations (e.g. MODIS, EARLINET, CALIPSO) and on high  
58 resolution modeling simulations. Assimilation of satellite derived Aerosol Optical Depth (AOD), has  
59 been shown to improve the dust forecasts in global models especially for the long range transport  
60 (Benedetti, et al., 2009); however this approach cannot be easily adopted for the description of  
61 haboobs. The reason is that the convective events and the associated wind gusts are not properly  
62 resolved at coarse model resolutions. As a result, assimilating the satellite AOD over an inaccurate



63 meteorological field does not improve the dust forecast.

64 A variety of studies on haboobs has been performed worldwide. Knippertz et al. (2009); Reinfried et  
65 al. (2009); Solomos et al. (2012); Roberts and Knippertz (2014), analyzed the physical processes that  
66 lead in severe haboob formation in Sahara as an aftermath of Atlas Mountains convective storms.  
67 Bou Karam et al. (2008) showed the contribution of the east Atlantic monsoon flow and the  
68 associated mesoscale convective systems (MCS) in dust elevation along the Sahel. Vukovic et al.  
69 (2014) described the severe convective dust storm that hit Phoenix Arizona in July 2011. Asian  
70 haboobs from the Taklimakan and Gobi deserts are described and simulated in Takemi, (1999,  
71 2005). All these studies agree in the complexity and synergy between various physical processes at  
72 multiple atmospheric scales that govern the generation and lifetime of these systems. Apart from  
73 their devastating effects at local and near surface scales, such events may also contribute to the  
74 free-troposphere dust burden in several ways: First, entrainment of dust particles in the free  
75 troposphere takes place at the turbulent region of the density current head (Takemi, 2005; Solomos  
76 et al., 2012); Second, they trigger secondary convective cells along their pathways that may evolve  
77 to synoptic scale dust events and third, dust residuals remain aloft after the cold pool declines.

78 The current article is the second part (Part 2) in a series of articles on the September 2015  
79 extraordinary dust storm in Middle East and Eastern Mediterranean. In Part 1, Mamouri et al.  
80 (2016) present a detailed analysis of remote sensing and in-situ monitoring of the event over  
81 Cyprus. The formation of similar events is not fully understood and we use this unique episode to  
82 elucidate the mechanism of dust production in this understudied region. EARLINET measurements  
83 along with CALIPSO and MSG observations are used to fine tune RAMS simulations and explain the  
84 physical processes that resulted in this haboob-driven dust storm. We focus our analysis on the first  
85 two days of the event (6 and 7 September 2015) when the extraordinary dust-storm was generated.  
86 To the best of our knowledge this is the first detailed modeling and remote sensing study to  
87 describe a Middle East haboob. The modeling and measurement techniques for the analysis are  
88 presented in Section 2. Section 3 includes the model results, the remote sensing observations and  
89 the investigation of the atmospheric processes that lead in the formation of the dust episode.  
90 Conclusive remarks and discussion are presented in Section 4.

91



92 **2. Instruments and models.**

93

94 **2.1 Remote sensing observations**

95 **2.1.1. EARLINET**

96 The lidar station at Limassol (34.7° N, 33° E; 23 m above sea level, a.s.l.) is part of the European  
97 Aerosol Research Lidar Network (EARLINET: Pappalardo et al., 2014). Details on the lidar station  
98 equipment and the retrieval algorithms are given in Mamouri et al. (2016). Dust mass concentration  
99 profiles are obtained from the dust optical properties following the methodology proposed by  
100 Ansmann et al. (2012). For this case study we use a lidar ratio of 40 sr that is typical for Middle East  
101 dust (Mamouri et al., 2013). The overall uncertainty in the estimated dust mass concentrations is  
102 20-30%.

103

104 **2.1.2. CALIPSO**

105 CALIOP, the principal instrument on board the CALIPSO satellite is a standard dual-wavelength (532  
106 and 1064 nm) backscatter lidar, operating a polarization channel at 532 nm (Winker et al., 2009).  
107 CALIOP has been acquiring high-resolution profiles of the attenuated backscatter at 532 and 1064  
108 nm along with polarized backscatter in the visible channel since 2006. After calibration and range  
109 correction of the lidar backscatter signals (Level 1 CALIPSO product), cloud and aerosol layers are  
110 identified and aerosol backscatter and extinction coefficient profiles at 532 and 1064 nm are  
111 retrieved as part of the Level 2 CALIPSO product. The CALIPSO algorithms are described in detail in a  
112 special issue of the Journal of Atmospheric and Oceanic Technology (e.g., Winker et al., 2009). In  
113 this study, we utilize L2 version 3 Aerosol and Cloud profiles product at a horizontal resolution of 5  
114 km analysis and vertical resolution of 60 m (in altitudes up to 8 km above sea level). In extreme  
115 haboob events, where the optical signal is very high, it is possible for the algorithm to wrongly  
116 attribute a dust layer as a cloud. In order to address this issue and fully understand the observed  
117 scene we use collocated information derived from MSG-SEVIRI (see sect. 2.1.3). In the two CALIPSO  
118 cases used here, MSG-SEVIRI RGB images confirmed that CALIPSO overpasses was cloud free, hence  
119 we classify both aerosol and cloud categorized CALIPSO observations as aerosol. Moreover, both of  
120 the cases have significantly high particle depolarization ratio values, which is a signature of pure  
121 dust scenes. In order convert the dust extinction coefficient from CALIPSO into dust mass  
122 concentration, we follow the methodology proposed by Ansmann et al. (2012) using the conversion



123 parameter of desert dust that is proposed in Mamouri and Ansmann (2017).

124

### 125 **2.1.3. MSG-SEVIRI**

126 The Meteosat dust RGB composite is produced from a combination between three MSG channels:  
127 IR12.0-IR10.8 (red), IR10.8-IR8.7 (green) and IR10.8 (blue). This product is provided in hourly  
128 intervals by EUMETSAT (European Organisation for the Exploitation of Meteorological Satellites)  
129 and aims in the monitoring of dust transport. Dust in these RGB images appears in pink or magenta  
130 colors while green-blue and red-brown colors are reserved for land and clouds respectively (Lensky  
131 and Rosenfeld, 2008).

132

## 133 **2.2 Modeling simulations**

### 134 **2.2.1 RAMS-ICLAMS model**

135 For the simulations used in this study we adopt the online coupled atmospheric and air quality  
136 modeling system RAMS-ICLAMS (Pielke et al., 1992; Meyers et al., 1997; Cotton et al., 2003;  
137 Solomos et al., 2011). The Integrated Community Limited Area Modeling System (ICLAMS) is an  
138 enhanced version of RAMS6.0 and it has been developed by the Atmospheric Modeling and  
139 Weather Forecasting Group at the University of Athens, Greece. The model is set up in a two-way  
140 nesting configuration. The external domain grid space is set at 12×12 km and the grid space of the  
141 inner domain is set at 4×4 km. A higher resolution (cloud resolving) grid at 2×2 km is nested over the  
142 haboob generation area at Syria-Iraq-Iran-Turkey borders. The locations of the model domains are  
143 shown in Figure 1b. The vertical structure of the model consists of 50 terrain following levels  
144 stretching from the surface up to 18 km. The dust production scheme follows the saltation and  
145 bombardment approach (Marticorena and Bergametti 1995; Spyrou et al., 2010). Wet and dry  
146 deposition of dust is formulated following Seinfeld and Pandis 1998. Mineral dust is represented  
147 with a transport mode of eight radii bins namely 0.15, 0.25, 0.45, 0.78, 1.3, 2.2, 3.8 and 7.1 μm. Sea  
148 salt aerosol is also parameterized following Monahan et al., 1986; Zhang et al., 2005; Leeuw et al.,  
149 2000 and Gong et al., 2002, 2003 and it is represented with an accumulated and a coarse mode at  
150 0.18 μm and 1.425 μm in radius respectively. Dust and sea salt particles interact with the radiative  
151 transfer code of the model (Rapid Radiative Transfer Model (RRTM), Mlawer et al., 1997; Iacono et  
152 al., 2000) for the computation of heating rate fluxes. The formation of cloud condensation nuclei  
153 (CCN) and ice nuclei (IN) from dust and sea salt particles is also included in the model based on the



154 schemes of Fountoukis and Nenes, 2005 and Barahona and Nenes 2009. Initial and boundary  
155 conditions are from the NCEP final analysis dataset (FNL at  $1^{\circ}\times 1^{\circ}$  resolution) and the sea surface  
156 temperature is the NCEP operational SST at  $0.5^{\circ}\times 0.5^{\circ}$ . The convective parameterization scheme of  
157 Kain and Fritsch, 1993 (KF) is activated for the two coarser grids. Assimilation of radiosonde data  
158 from the airports of Adana ( $36.98^{\circ}\text{N}$ ,  $35.35^{\circ}\text{E}$ ), Bet Dagan ( $32.00^{\circ}\text{N}$ ,  $34.81^{\circ}\text{E}$ ), Diyarbakir ( $37.54^{\circ}\text{N}$ ,  
159  $40.12^{\circ}\text{E}$ ), Mafraq ( $32.36^{\circ}\text{N}$ ,  $36.25^{\circ}\text{E}$ ) and Nicosia ( $35.10^{\circ}\text{N}$ ,  $33.30^{\circ}\text{E}$ ) is also activated to fine tune the  
160 simulations. A series of sensitivity runs with various model configurations (different physical  
161 schemes, assimilation parameters and domain structures) is performed until we conclude to the  
162 optimum setup for the specific simulation.

163

#### 164 **2.2.2 Land use changes and activation of dust sources**

165 An accurate representation of dust sources in the region is crucial for understanding this complex  
166 dust event, but this is hampered by recent land cover changes in the region. The original land use  
167 database of the model is the USGS Data Base Version 2 which is obtained from 1-km AVHRR data  
168 (Advanced Very High Resolution Radiometer) spanning April 1992 through March 1993. However,  
169 complex interactions of drier climate (Notaro et al., 2015; Cook et al., 2016), transboundary water  
170 managements (Voss et al. 2013), and prolonged conflict (Jaafar and Woertz, 2016) have led to  
171 change of land use types that are no longer reflected at the model and this could have a large  
172 impact on dust production. The comparison of Landsat 8 natural color and NDVI imagery between  
173 2013 and 2015 (Figure 2) reveals large areas of uncultivated fields in regions of contested borders  
174 and exposed river and lake-bed sediments especially around the Euphrates river, all of which are  
175 known to be very efficient dust sources (Prospero et al, 2002; Ginoux et al., 2012). In order to get  
176 most accurate representation of dust sources for the specific event we use 1km monthly  
177 Normalized Difference Vegetation Index (NDVI) from MODIS (Didan K., 2015) to characterize land  
178 use type in the region of interest. Specifically, we consider regions with NDVI values from 0 to 0.1  
179 correspond to bare soil and consequently efficient dust sources (DeFries et al., 1994). The updated  
180 land cover dataset is used for all results shown in this study. Results from simulations using the  
181 older database are only shown in Figure 11 for comparison.

182

183

184



### 185 3. Results

#### 186 3.1 Meteorological conditions

187 The main driving force for the generation of this extreme dust episode is the combination between  
188 two distinct meteorological features in the greater area: (i) establishment of a thermal low over the  
189 bare-soil areas of Syria and (ii) convective outflow boundaries at the mountains of Iraq and Syria.  
190 These processes are analyzed in the following sections using modeling results and remote sensing  
191 observations.

##### 192 3.1.1 Development of a low pressure system over Syria on 6 September 2015

193 As seen at the outer model grid in Figure 1a, the passage of a trough is evident over Turkey on 6  
194 September 2015, 00:00 UTC. The low pressure center at 500mb is found at 5840 m over the east  
195 bank of Black Sea. During the same day, radiative warming of the bare soil surface results in very  
196 hot soil temperatures exceeding 50 °C in Syria and Iraq. This combination of cold air aloft with low  
197 level warming, leads in the formation of a thermal low pressure system over Syria. Another  
198 parameter that plays important role for the process of dust source activation is the difference  
199 between surface temperature ( $T_{\text{Surf}}$ ) and air temperature at 2m ( $T_{2\text{m}}$ ). Findings from earlier field  
200 experiments (i.e. SAMUM) show that such a difference of 17°C-20°C facilitates the uplift of  
201 convective dust plumes (Ansmann et al., 2009). As seen in Figure 1b, the modeled  $T_{\text{Surf}}-T_{2\text{m}}$   
202 difference at 10:00 UTC exceeds 17°C over extended bare soil areas in Syria. This temperature  
203 gradient further explains the effectiveness of dust production at these areas. The pressure system  
204 and the associated cyclonic flow persist during the entire day of 6<sup>th</sup> September 2015 and result in  
205 the mobilization of dust in the area. The low pressure system is evident by the 850 mb geopotential  
206 height contours in Figure 3a, reaching a minimum of 1490 m at 08:00 UTC, 6 September 2015. Dust  
207 uptake is mostly evident at the outer parts of the cyclone where surface wind speed exceeds  $7 \text{ m s}^{-1}$   
208 almost during the entire day and  $T_{\text{Surf}}-T_{2\text{m}}$  obtains maximum values. The elevated particles are  
209 quickly distributed inside the system and a distinct cylindrical dust cloud is soon formed.  
210 Recirculation of the elevated dust particles inside the closed cyclonic flow results in extreme AOT  
211 values exceeding 15 at specific areas as seen in Figure 3a. The formation of this dense dust plume is  
212 also evident in the MSG-SEVIRI satellite dust RGB image in Figure 3b. Pink and purple colors in this  
213 image indicate dust while brown and red colors indicate clouds. As seen in Figure 4, convergence of  
214 low level flow along the Mediterranean coastline during the morning hours on September 6<sup>th</sup>,  
215 results in local convective activity at the area of Lebanon Mountains and in local disturbance of the



216 mesoscale wind field. A SE flow is established, and this flow is responsible for the transport of dust  
217 from Lebanon towards Cyprus that is evident at the satellite and modeling images on 7 September  
218 2015, 00:00 UTC (Figure 5). This cut-off plume (plume\_1) travels in the lower troposphere above  
219 the marine boundary layer and it was observed at 1.5 km above Limassol at 19:00 UTC on  
220 September 7<sup>th</sup> as reported by Mamouri et al., 2016. The faster propagating haboob plume  
221 (plume\_2) also was detected at 2.0-3.5 km over Cyprus at 19:00 UTC. The extreme AOT values (>10)  
222 that are seen in Figure 5a over Syria result from the overlapping of cyclone-driven and haboob-  
223 driven dust over this area. In the model, approaching of the haboob front in Syria is accompanied  
224 also by cloud formation as seen by the 70% cloud-cover contours in Figure 5a; however these clouds  
225 are not evident in the satellite image (Figure 5b). The more elevated (cyclone-driven) dust in Figure  
226 5b is shown in pink (plume\_1 over the sea and plume\_3 over North Syria and South Turkey have the  
227 same origin) and the near surface dust (haboob) is shown with a darker purple color (plume\_2).

228

### 229 **3.1.2. Convection and haboob generation on 6 and 7 September 2015**

230 At 13:00 UTC on 6<sup>th</sup> of September a northward low level flow is evident over N. Iraq and N. Syria  
231 (Figure 6a). This relatively unstable air mass is characterized by increased equivalent potential  
232 temperature ( $\theta_e$ ) reaching up to 508 K. This flow is associated with a westerly shift of the  
233 Somalian Low Level Jet (SLLJ). The SLLJ is part of the West India Monsoon circulation and as shown  
234 in Figure 6b it is characterized by strong SW winds blowing from the Somalia highlands towards  
235 West India. This low level flow steers towards the west along the coastal mountains of Yemen and  
236 Oman and results in SE winds transferring moisture from the Arabian Sea towards the inlands of the  
237 Arabian Peninsula. Mechanical elevation of this relatively unstable air as it approaches Mt. Sinjar in  
238 N. Iraq (Figure 6a) triggers convection at this area. A crucial parameter that determines the  
239 formation of a cold pool is the temperature difference between rain droplets and the ambient air.  
240 As seen in Figure 7a, the absolute difference between rain droplets temperature and ambient air  
241 temperature in the model reaches a maximum of 22 °C at this area. This temperature gradient  
242 results in a faster evaporation rate of the rain droplets as they fall through the unsaturated air and  
243 in the formation of a cold pool at the area of North Iraq. Wind speed inside the cold pool ranges  
244 from 10 up to 20  $\text{ms}^{-1}$  (Figure 7b). This cold pool moves towards the North and triggers the  
245 generation of secondary convective cells at the mountainous areas along Iran-Iraq-Turkey  
246 borderline. At 20:00 UTC, a series of convective outflows converges in an organized SE propagating





247 density current that is evident in the model over N. Iraq and N. Syria (Figure 8a). This system is  
248 characterized by wind speeds higher than  $6 \text{ m s}^{-1}$  and results in activation of dust sources and near  
249 surface concentrations largely exceeding  $10000 \mu\text{g m}^{-3}$  (Figure 8b). However, the corresponding  
250 SEVIRI image (Figure 8c) indicates that by this time the haboob has already penetrated about 200  
251 km inside Syria which is not reproduced by the model. This latency between satellite and modeled  
252 haboob fronts is an indication that the convective downdrafts were in fact even stronger.

253

## 254 **3.2 Dust cloud properties and comparison with observations**

### 255 **3.2.1. Vertical dust structure**

256 The dust layer structure as it propagates towards the Mediterranean is captured by two CALIPSO  
257 overpasses at 23:33 UTC, 6 September 2015 (Figure 9) and at 10:35 UTC, 7 September 2015 (Figure  
258 10). Collocated model cross sections of dust and MSG-SEVIRI dust images are also presented in  
259 Figures 8 and 9. All heights in satellite and model profiles refer to heights above surface. At the first  
260 overpass (Figure 9), the south part of the dust layer ( $31^{\circ}\text{N}$ - $34^{\circ}\text{N}$ ) is detected up to 2-3 km and  
261 originates from the cyclonic flow over Syria. Dust concentrations are estimated from CALIPSO  
262 backscatter and as seen in Figure 9b they reach up to  $5000 \mu\text{g m}^{-3}$  close to the surface between  
263  $31^{\circ}\text{N}$ - $34^{\circ}\text{N}$  and higher than  $6000 \mu\text{g m}^{-3}$  in the first 500 m. Similar structure and dust concentrations  
264 are also found by the model (Figure 9c). The northern part of the overpass ( $35^{\circ}\text{N}$ - $38^{\circ}\text{N}$ ) detects also  
265 elevated dust due to cyclonic activity between 2.5-4.5 km and concentrations up to 1000-2000  $\mu\text{g m}^{-3}$   
266 are evident at this area from CALIPSO. The model overpredicts dust at this area with simulated  
267 concentrations reaching up to  $5000 \mu\text{g m}^{-3}$ . These elevated layers are shown with pink colors in  
268 Figure 9a. Low level dust (purple colors in SEVIRI images) is also evident in this area due to the  
269 propagating haboob and CALIPSO detects this two-layer structure with a clear separation at 2 km.  
270 The model also reproduces the uplift of dust at  $35^{\circ}\text{N}$  where the two systems (cyclone and haboob)  
271 merge. The modeled concentration inside the haboob reaches extraordinary values exceeding  
272  $10000 \mu\text{g m}^{-3}$ . Due to the severity of the event, the CALIPSO lidar signal is totally attenuated below  
273  $\sim 1 \text{ km}$  (dark blue color), in the area between  $35^{\circ}\text{N}$ - $37^{\circ}\text{N}$ . For that reason the information from the  
274 satellite is limited there in the highest 500m of the propagated haboob, implying also the existence  
275 of much higher values close to the surface.

276 The second overpass at 7 September 10:35 UTC is actually behind or at the tail of the propagating  
277 dust storm (Figure 10a). The thin dust layer that is detected by CALIPSO between  $30^{\circ}\text{N}$ - $32^{\circ}\text{N}$  reaches



278 up to 2 km and maximum dust concentrations of up to 2000-3000  $\mu\text{g m}^{-3}$  are calculated mostly close  
279 to the surface (Figure 10b). Extreme dust concentrations are also found in both satellite and model  
280 plots between 34°N-36°N at the tail of the propagating system. Dust values at this area are so high  
281 that CALIPSO observation suffers again from total attenuation of the lidar signal after penetrating  
282 the first 1000 m and extraordinary concentrations of up to 20000  $\mu\text{g m}^{-3}$  are found in the lower  
283 model levels (up to 1.5 km). Similar values are observed from CALIPSO in the edge of the haboob  
284 (33.5°N-34°N) where the signal is strong enough to provide valuable information. The elevated  
285 layers (2-4 km) between 36°N-38°N at both CALIPSO and model profiles are dust residuals over the  
286 mountains of Turkey. An elevated dust layer of up to 600  $\mu\text{g m}^{-3}$  is also found south of 35°N in the  
287 model at heights between 3-4 km. Due to the aforementioned latency between the true and  
288 modeled propagation speeds, the model cross-section is closer to the core of the system hence this  
289 layer consists of modeled cyclone uplifted dust that in fact is already west of the CALIPSO track.  
290

### 291 3.2.2. Dust load over Cyprus

292 The observed structure and amounts of dust arriving in Cyprus is described in detail by Mamouri et  
293 al. (2016). The arrival of the dust plumes at Limassol in Cyprus is evident in Figure 11. A double layer  
294 structure is detected by the lidar at 7 September 19:00 UTC. The relatively shallow dust layer that is  
295 found between 0.8-1.7 km with a maximum peak at 2000  $\mu\text{g m}^{-3}$ , comes from the detached dust air  
296 mass traveling off the coast of Libanon as described in Section 3.1.1. The model reproduces  
297 correctly the height of this layer but the maximum concentration is underestimated by almost 50 %.  
298 The upper layer that is detected between 1.8-3.6 km originates from the north part of the fast  
299 propagating haboob that catches up with the “Lebanon” dust over Cyprus. The location and dust  
300 concentrations of this layer are adequately reproduced by the model. The total modeled dust load  
301 is similar to the observed (lidar) dust load but the vertical distribution of dust in two distinct layers  
302 is not so clearly reproduced. Model results using the old vegetation database are also shown in  
303 Figure 11. As seen by the dashed line in this plot, this simulation failed to reproduce the strength of  
304 the event and the maximum concentration is 400  $\mu\text{g m}^{-3}$  at about 0.7 km height. On the 8<sup>th</sup> of  
305 September the lidar system could not operate due to the extraordinary dust load. The mean MODIS  
306 derived AOT on this day varied between 1.5-5 over five sites in Cyprus (Pafos, Limassol, Larnaca,  
307 Nicosia, Rizokarpaso), (Mamouri et al., 2016). Given the fact that the maximum retrievable MODIS  
308 AOT is 5, these values are most probably an underestimation of the true AOT. The distribution of



309 modeled AOT during 00:00 UTC-15:00 UTC on the 8<sup>th</sup> of September is shown in Figure12; the dust  
310 plume approaches Cyprus from the South and the orographic effect of Mt. Troodos results in an  
311 inhomogeneous distribution of dustload over the island, which explains the AOT variability between  
312 the sites. The modeled AOT values over the Middle East inland exceed 10 as shown also by the  
313 sharp gradient towards the eastern part of Figure 12 plots. However the extreme dust storm  
314 affecting Cyprus during the 8<sup>th</sup> of September is the result of a plume that approaches the island  
315 from the south. This dust layer is evident between 1.5-3.5 km in the vertical cross-sections of model  
316 dust concentration at 00:00 UTC and 03:00 UTC in Figure 13. Downward mixing of dust as this air  
317 mass approaches the topographic barrier of Troodos mountain increases the near-surface  
318 concentrations at the southern sites especially during local morning and noon hours (06:00 UTC,  
319 09:00 UTC). In the afternoon hours (12:00 UTC, 15:00 UTC), the development of upward motions  
320 over Mt. Troodos separates the dust flow over Cyprus into two distinct cells (a south and a north  
321 one) and at this time increased concentrations are found over the northern sites of the island. The  
322 maximum simulated concentrations are up to 4000  $\mu\text{g m}^{-3}$  aloft and about 1000  $\mu\text{g m}^{-3}$  close to the  
323 surface. Taking into account the complexity of the situation, the spatiotemporal evolution of the  
324 episode seems to be correctly explained by the model but the extreme values of 8000-10000  $\text{mg m}^{-3}$   
325 that are reported by Mamouri et al. (2016) are not reproduced. This discrepancy can be attributed  
326 to a variety of reasons related to both dust and atmospheric properties that are not properly  
327 resolved even at this fine model scale (e.g. more intense downward mixing or increased emissions  
328 from the sources). The modeled versus observed maximum AOT values for the five sites are also  
329 shown in Table 1. The model reproduces the higher AOTs at the most southern sites (Limassol and  
330 Pafos) compared to the central and north sites. Following the previous discussion about the already  
331 underestimated MODIS AOT it seems that the model reproduces the distribution of dust over  
332 Cyprus however with an overall underestimation of more than 2. A possible explanation could be  
333 also that the dry river beds of Tigris and Euphrates as well as several dust sources over Syria and  
334 North Iraq provide even more erodible sediments than those assumed by the model hence the  
335 discrepancies in dust concentrations.

336

337

338

339



340 Table 1. Maximum MODIS and RAMS AOT over Cyprus, 8 September 2015

	Pafos	Limassol	Larnaca	Nicosia	Rizokarpaso
MODIS <sub>AOT</sub>	3.5	5.0	5.0	2.0	5.0
RAMS <sub>AOT</sub>	3.5	4.0	3.0	3.0	3.0

341

342

#### 343 4. Discussion and Conclusions

344 A combination of meteorological and landuse conditions resulted in the formation of an  
345 unprecedented dust episode over Middle East and East Mediterranean during 6-11 September  
346 2015. This event is unique due to the coincidence of various atmospheric phenomena related with  
347 the generation of turbulence and dust production. Interpretation and analysis of remote sensing  
348 data (EARLINET, CALIPSO, MSG-SEVIRI) and modeling simulations (RAMS-ICLAMS) reveals the main  
349 reasons that led in the uplift and persistence of the dust layers. The major processes affecting the  
350 generation of the dust storm are found to be:

- 351 1. The formation of a strong thermal low over Syria that lifted dust up to 4 km.
- 352 2. The intrusion of a moist and unstable air mass from the Arabian Sea that triggered  
353 convective activity over Iraq-Iran-Syria-Turkey borderline.
- 354 3. The generated outflow boundaries that led in dust deflation and formed a westward  
355 propagating haboob merging with the previously elevated dust over Syria.
- 356 4. The efficiency of Middle East dust sources is increased as an aftermath of war and the  
357 related changes in land use.

358 As reported by Mamouri et al. (2016), almost all operational dust models failed to forecast this  
359 event. RAMS-ICLAMS in this study is not used in forecasting mode but rather as a tool for the a-  
360 posteriori analysis and explanation of the event. This means that the configuration of several model  
361 parameters such as the nested grid structure, convective parameterization schemes, dust source  
362 strength etc. is guided by the available observations. In this context, most observed processes are  
363 successfully described by the model and the various physical mechanisms that took place during the  
364 event are explained. However, certain inaccuracies in the quantification of atmospheric variables  
365 and spatiotemporal deviations in the description of convection and other physical processes can still  
366 significantly decrease the model skill especially regarding the quantification of dust mass profiles.



367 The analysis presented here raises considerations regarding the forecast skills of the atmospheric  
368 dust models, since even though such extreme episodes are very seldom they still represent the  
369 most threatening dust hazards. The long range transport and the general circulation of dust in the  
370 atmosphere are nowadays adequately forecasted by most global models but convectively driven  
371 episodes cannot be resolved at synoptic and mesoscale resolutions. Moreover, a recent study by  
372 Pope et al., 2016 suggests that unresolved haboobs may be responsible for up to 30% of the total  
373 atmospheric dust and such considerations raise questions on the current status of early warning  
374 systems for dust episodes. It is probably obvious that such a system cannot rely exclusively on  
375 modeling simulations. As shown at the present study, the complexity of these events makes their  
376 forecast very challenging and even at convection permitting resolutions, it is possible that a certain  
377 model configuration could successfully reproduce a specific event but not all similar events.  
378 Moreover, such high resolution grid-space can only be applied over limited areas due to restrictions  
379 in computational power.

380 Remote sensing observations can play an important role for the provision of more accurate dust  
381 forecasts. Engagement of geostationary satellite observations (MSG, Sentinel-4) and CALIPSO  
382 profiles in forecasting activities could improve the forecasting skill either by the direct assimilation  
383 of satellite data in dust models or by issuing human-assisted early warnings. Expansion of a lidar  
384 network close to dust source areas (e.g. Sahara, Middle East) will also complement model activities  
385 through the provision of ground truth observations for the vertical profile of dust plumes.  
386 Additionally, the activation of synchronous observations from the EARLINET network following a  
387 dust forecast notice will allow a closer investigation of the physical processes that drive these  
388 events

389

390 .

391

### 392 **Acknowledgements**

393 The authors acknowledge support through the following projects and research programs: BEYOND  
394 under grant agreement no. 316210 of the European Union Seventh Framework Programme FP7-  
395 REGPOT-2012-2013-1. ACTRIS-2 under grant agreement no. 654109 of the European Union's  
396 Horizon 2020 research and innovation programme. ECARS under grant agreement No 602014 from  
397 the European Union's Horizon 2020 Research and Innovation programme. MarcoPolo under grant



398 agreement no. 606953 of the European Union Seventh Framework Programme FP7/2007-2013. The  
399 authors acknowledge EARLINET for providing aerosol lidar profiles available under the World Data  
400 Center for Climate (WDCC) (The EARLINET publishing group 2000-2010, 2014a. CALIPSO data were  
401 obtained from the ICARE Data Center (<http://www.icare.univ-lille1.fr/>) and from the NASA Langley  
402 Research Center Atmospheric Science Data Center. CALIPSO data were provided by NASA. We thank  
403 the ICARE Data and Services Center for providing access to the data used in this study and their  
404 computational center.

405

406 **References**

407

408 Ansmann A., Tesche, M., Knipperts, P., Bierwirth, E., Althausen, D., Müller, D. and Schulz, O.: Vertical profiling  
409 of convective dust plumes in southern Morocco during SAMUM. *Tellus* 61B, doi:10.1111/j.1600-  
410 0889.2008.00384.x., 2009

411 Ansmann, A., Petzold, A., Kandler, K., Tegen, I., Wendisch, M., Müller, D., Weinzierl, B., Müller, T., and  
412 Heintzenberg, J.: Saharan Mineral Dust Experiments SAMUM-1 and SAMUM-2: what have we learned?,  
413 *Tellus*, 63B, 403–429, 2011

414 Ansmann, A., Seifert, P., Tesche, M., and Wandinger, U.: Profiling of fine and coarse particle mass: case  
415 studies of Saharan dust and Eyjafjallajökull/Grimsvötn volcanic plumes, *Atmos. Chem. Phys.*, 12, 9399–  
416 9415, doi:10.5194/acp-12-9399-2012, 2012.

417 Barahona, D., West, R. E. L., Stier, P., Romakkaniemi, S., Kokkola, H., and Nenes, A.: Comprehensively  
418 accounting for the effect of giant CCN in cloud activation parameterizations, *Atmos. Chem. Phys.*, 10,  
419 2467–2473, doi:10.5194/acp-10-2467-2010, 2010.

420 Benedetti A., J.-J., Morcrette, O. Boucher, A. Dethof, R. J. Engelen, M. Fisher, H. Flentje, N. Huneeus, L. Jones,  
421 J. W. Kaiser, S. Kinne, A. Mangold, M. Razinger, A. J. Simmons, and M. Suttie: Aerosol analysis and forecast  
422 in the European Centre for Medium-Range Weather Forecasts Integrated Forecast System: 2. Data  
423 assimilation, *J. Geophys. Res.*, 114, D13205, doi:10.1029/2008JD011115., 2009

424 Bou Karam, D., Flamant, C., Knippertz, P., Reitebuch, O., Pelon, J., Chong, M., and Dabas, A: Dust emissions  
425 over the Sahel associated with the West African Monsoon inter-tropical discontinuity region: a  
426 representative case study, *Q. J. Roy. Meteor. Soc.*, 134, 621–634, 2008.

427 Cook, B. I., Anchukaitis, K. J., Touchan, R., Meko, D. M. and Cook, E. R.: Spatiotemporal drought variability in  
428 the Mediterranean over the last 900 years, *J. Geophys. Res. Atmos.*, 121(5), 2015JD023929,  
429 doi:10.1002/2015JD023929, 2016.

430 Cotton W. R., Pielke Sr., R. A., Walko, R. L., Liston, G. E., Tremback, C. J., Jiang, H., McAnelly, R. L., Harrington,  
431 J. Y., Nicholls, M. E., Carrio, G. G., and McFadden, J. P.: RAMS 2001: Current status and future directions,



- 432 Meteor. Atmos. Phys., 82, 5–29, 2003
- 433 DeFries, R. S. and Townshend, J. R. G.: NDVI-derived land cover classifications at a global scale, International  
 434 Journal of Remote Sensing, 15(17), 3567–3586, doi:10.1080/01431169408954345, 1994.
- 435 Didan, K: MOD13A3 MODIS/Terra vegetation Indices Monthly L3 Global 1km SIN Grid V006, ,  
 436 doi:10.5067/MODIS/MOD13A3.006, 2015.
- 437 Emmel C, Knippertz P, Schulz O (2010) Climatology of convective density currents in the southern  
 438 foothills of the Atlas mountains. J Geophys Res 115, D11115. doi:10.1029/2009JD011819
- 439 Fountoukis, C., Nenes, A., Meskhidze, N., Bahreini, R., Conant, W. C., Jonsson, H., Murphy, S., Sorooshian, A.,  
 440 Varutbangkul, V., Brechtel, F., Flagan, R. C., and Seinfeld, J. H.: Aerosol – cloud drop concentration closure  
 441 for clouds sampled during the International Consortium for Atmospheric Research on Transport and  
 442 Transformation 2004 campaign, J. Geophys. Res., 112, D10S30, doi:10.1029/2006JD007272, 2007.
- 443 Ginoux, P., Prospero, J. M., Gill, T. E., Hsu, N. C. and Zhao, M.: Global-scale attribution of anthropogenic and  
 444 natural dust sources and their emission rates based on MODIS Deep Blue aerosol products, Rev.  
 445 Geophys., 50(3), RG3005, doi:10.1029/2012RG000388, 2012.
- 446 Gong, S. L., Barrie, L. A., and Lazare, M.: Canadian Aerosol Module (CAM): a size-segregated simulation of  
 447 atmospheric aerosol processes for climate and air quality models. 2. Global seasalt aerosol and its  
 448 budgets, J. Geophys. Res., 107(D24), 4779, doi:10.1029/2001JD002004, 2002.
- 449 Gong, S. L.: A parameterization of sea-salt aerosol source function for sub- and super-micron particles, Global  
 450 Biogeochem. Cy., 17, 1097, doi:10.1029/2003GB002079, 2003.
- 451 Iacono, M. J., Mlawer, E. J., Clough, S. A., and Morcrette, J. J.: Impact of an improved longwave radiation  
 452 model, RRTM, on the energy budget and thermodynamic properties of the NCAR Community Climate  
 453 Model, CCM3, J. Geophys. Res., 105, 14873– 14890, 2000
- 454 Jaafar, H. H. and Woertz, E.: Agriculture as a funding source of ISIS: A GIS and remote sensing analysis, Food  
 455 Policy, 64, 14–25, doi:10.1016/j.foodpol.2016.09.002, 2016.
- 456 Kain, J. S. and Fritsch, J. M.: Convective parameterization for mesoscale models: The Kain-Fritsch scheme. The  
 457 representation of cumulus convection in numerical models, Meteor. Monogr., No. 24, Amer. Meteor.  
 458 Soc., 165–170, 1993.
- 459 Knippertz P, Trentmann J, Seifert A., High resolution simulations of convective cold pools over the  
 460 northwestern Sahara. J. Geophys. Res. 2009; 114:D21109. doi: 10.1029/2007JD008774., 2009
- 461 Leeuw, G., Neele, F. P., Hill, M., Smith, M. H., and Vignali, E.: Production of sea spray aerosol in the surf zone,  
 462 J. Geophys. Res.- Atmos., 105, 29397–29409, 2000.
- 463 Lensky I.M. and D. Rosenfeld, 2008: Clouds-Aerosols-Precipitation Satellite Analysis Tool (CAPSAT). Atmos.  
 464 Chem. Phys., 8, 6739–6753.
- 465 Mamouri, R. E., Ansmann, A., Nisantzi, A., Kokkalis, P., Schwarz, A., and Hadjimitsis, D.: Low Arabian dust



- 466 extinction-to-backscatter ratio, *Geophys. Res. Lett.*, 40, 4762–4766, doi:10.1002/grl.50898, 2013.
- 467 Mamouri R.E., Ansmann, A., Nisantzi, A., Solomos, S., Kallos, G., and Hadjimitsis, D.G.: Extreme dust storm  
468 over the eastern Mediterranean in September 2015: satellite, lidar, and surface observations in the  
469 Cyprus region *Atmos. Chem. Phys.*, 16, 1–14, 2016 [www.atmos-chem-](http://www.atmos-chem-phys.net/16/1/2016/doi:10.5194/acp-16-1-2016)  
470 [phys.net/16/1/2016/doi:10.5194/acp-16-1-2016](http://www.atmos-chem-phys.net/16/1/2016/doi:10.5194/acp-16-1-2016).
- 471 Mamouri, R.E. and Ansmann, A.: Fine and coarse dust separation with polarization lidar: Extended  
472 Methodology for multiple wavelengths, to be submitted to ACP, 2017.
- 473 Marsham, J. H., N. S. Dixon, L. Garcia-Carreras, G. M. S. Lister, D. J. Parker, P. Knippertz, and C. E. Birch : The  
474 role of moist convection in the West African monsoon system: Insights from continental-scale convection-  
475 permitting simulations, *Geophys. Res. Lett.*, 40, 1843–1849, doi:10.1002/grl.50347., 2013
- 476 Marticorena, B. and Bergametti, G.: Modeling the atmospheric dust cycle: 1. Design of a soil derived dust  
477 emission scheme, *J. Geophys. Res.*, 100, 16415–16430, 1995.
- 478 Meyers, M. P., Walko, R. L., Harrington, J. Y., and Cotton, W. R: New RAMS cloud microphysics  
479 parameterization. Part II: The two-moment scheme, *Atmos. Res.*, 45, 3–39, 1997
- 480 Mlawer, E. J., Taubman, S. J., Brown, P. D., Iacono, M. J., and Clough, S. A.: Radiative transfer for  
481 inhomogeneous atmospheres: RRTM, a validated correlated-k model for the longwave, *J. Geophys. Res.*,  
482 102(D14), 16663–16682, 1997.
- 483 Monahan, E. C., Spiel, D. E., and Davidson, K. L.: A model of marine aerosol generation via whitecaps and  
484 wave disruption, in: *Oceanic Whitecaps*, edited by: Monahan, E. C. and Mac Niocaill, G., D. Reidel, 167–  
485 174, 1986.
- 486 Notaro, M., Yu, Y. and Kalashnikova, O. V.: Regime shift in Arabian dust activity, triggered by persistent  
487 Fertile Crescent drought, *J. Geophys. Res. Atmos.*, 120(19), 2015JD023855, doi:10.1002/2015JD023855,  
488 2015.
- 489 Pielke, R. A., Cotton, W. R., Walko, R. L., Tremback, C. J., Lyons, W. A., Grasso, L. D., Nicholls, M. E., Moran, M.  
490 D., Wesley, D. A., Lee, T. J., and Copeland, J. H.: A comprehensive meteorological modeling system –  
491 RAMS, *Meteorol. Atmos. Phys.*, 49, 69–91, 1992.
- 492 Pope, R. J., J. H. Marsham, P. Knippertz, M. E. Brooks, and A. J. Roberts: Identifying errors in dust models  
493 from data assimilation, *Geophys. Res. Lett.*, 43, 9270–9279, doi:10.1002/2016GL070621., 2016
- 494 Prospero, J. M., Ginoux, P., Torres, O., Nicholson, S. E. and Gill, T. E.: Environmental Characterization of  
495 Global Sources of Atmospheric Soil Dust Identified with the Nimbus 7 Total Ozone Mapping Spectrometer  
496 (toms) Absorbing Aerosol Product, *Rev. Geophys.*, 40(1), 1002, doi:10.1029/2000RG000095, 2002.
- 497 Reinfried, F., I. Tegen, B. Heinold, O. Hellmuth, K. Schepanski, U. Cubasch, H. Huebener, and P. Knippertz :  
498 Simulations of convectively-driven density currents in the Atlas region using a regional model: Impacts on  
499 dust emission and sensitivity to horizontal resolution and convection schemes, *J. Geophys. Res.*, 114,

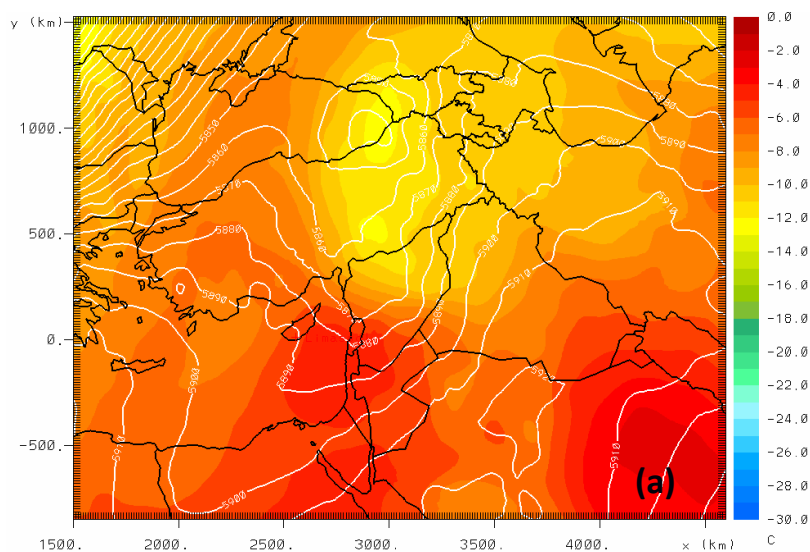




- 500 D08127, doi:10.1029/2008JD010844., 2009
- 501 Roberts, A. J., P. Knippertz : The formation of a large summertime Saharan dust plume: Convective and  
502 synoptic-scale analysis, *J. Geophys. Res. Atmos.*, 119, 1766–1785, doi:10.1002/2013JD020667., 2014
- 503 Ryder, C. L., McQuaid, J. B., Flamant, C., Rosenberg, P. D., Washington, R., Brindley, H. E., Highwood, E. J.,  
504 Marsham, J. H., Parker, D. J., Todd, M. C., Banks, J. R., Brooke, J. K., Engelstaedter, S., Estelles, V.,  
505 Formenti, P., Garcia-Carreras, L., Kocha, C., Marenco, F., Sodemann, H., Allen, C. J. T., Bourdon, A., Bart,  
506 M., Cavazos-Guerra, C., Chevaillier, S., Crosier, J., Darbyshire, E., Dean, A. R., Dorsey, J. R., Kent, J.,  
507 O’Sullivan, D., Schepanski, K., Szpek, K., Trembath, J., and Woolley, A.: Advances in understanding mineral  
508 dust and boundary layer processes over the Sahara from Fennec aircraft observations, *Atmos. Chem.*  
509 *Phys.*, 15, 8479–8520, doi:10.5194/acp-15-8479- 2015, 2015
- 510 Schepanski, K., Tegen, I., Todd, M. C., Heinold, B., Bonisch, G., Laurent, B., and Macke, A.: Meteorological  
511 processes forcing Saharan dust emission inferred from MSG-SEVIRI observations of subdaily dust source  
512 activation and numerical models, *J. Geophys. Res.*, 114, D10201, doi:10.1029/2008JD010325, 2009.
- 513 Seinfeld, J. H. and Pandis, S. N.: *Atmospheric Chemistry and Physics: From Air Pollution to Climate Change*, J.  
514 Wiley, New York, 1998
- 515 Solomos, S., Kallos, G., Kushta, J., Astitha, M., Tremback, C., Nenes, A., and Levin, Z.: An integrated modeling  
516 study on the effects of mineral dust and sea salt particles on clouds and precipitation, *Atmos. Chem.*  
517 *Phys.*, 11, 873–892, doi:10.5194/acp- 11-873-2011, 2011
- 518 Solomos, S., Kallos, G., Mavromatidis, E., and Kushta, J.: Density currents as a desert dust mobilization  
519 mechanism, *Atmos. Chem. Phys.*, 12, 11199–11211, doi:10.5194/acp-12-11199-2012, 2012.
- 520 Spyrou, C., Mitsakou, C., Kallos, G., Louka, P., and Vlastou, G.: An improved limited-area model for describing  
521 the dust cycle in the atmosphere, *J. Geophys. Res.*, 115, D17211, doi:10.1029/2009JD013682, 2010.
- 522 Takemi, T.: Explicit simulations of convective-scale transport of mineral dust in severe convective weather, *J.*  
523 *Meteorol. Soc. Jpn.*, 83A, 187–203, 2005.
- 524 Takemi, T.: Structure and evolution of a severe squall line over the arid region in Northwest China. *Mon.*  
525 *Wea. Rev.*, 127, 1301–1309., 1999.
- 526 The EARLINET publishing group 2000–2010: Adam, M., Alados-Arboledas, L., Althausen, D., Amiridis, V.,  
527 Amodeo, A., Ansmann, A., Apituley, A., Arshinov, Y., Balis, D., Belegante, L., Bobrovnikov, S., Boselli, A.,  
528 Bravo-Aranda, J. A., Bösenberg, J., Carstea, E., Chaikovskiy, A., Comerón, A., D’Amico, G., Daou, D.,  
529 Dreischuh, T., Engelmann, R., Finger, F., Freudenthaler, V., Garcia-Vizcaino, D., García, A. J. F., Geiß, A.,  
530 Giannakaki, E., Giehl, H., Giunta, A., de Graaf, M., Grana-dos-Muñoz, M. J., Grein, M., Grigorov, I., Groß, S.,  
531 ruening, C., Guerrero-Rascado, J. L., Haeffelin, M., Hayek, T., Iarlori, M., Kanitz, T., Kokkalis, P., Linné, H.,  
532 Madonna, F., Mamouri, R.-E., Matthias, V., Mattis, I., Menéndez, F. M., Mitev, V., Mona, L., Morille, Y.,  
533 Muñoz, C., Müller, A., Müller, D., Navas-Guzmán, F., Nemuc, A., Nicolae, D., Pandolfi, M., Papayannis, A.,



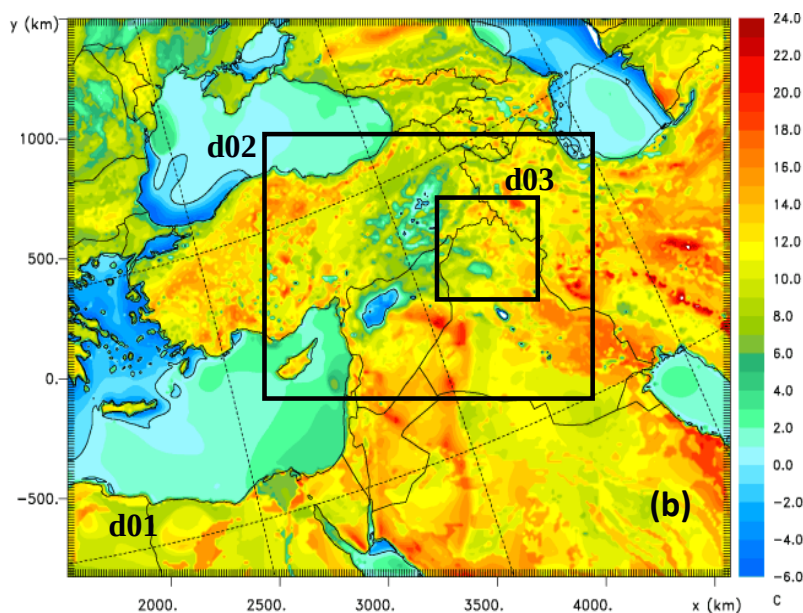
- 534 Pappalardo, G., Pelon, J., Perrone, M. R., Pietruczuk, A., Pisani, G., Potma, C., Preißler, J., Pujadas, M.,  
535 Putaud, J., Radu, C., Ravetta, F., Reigert, A., Rizi, V., Rocadenbosch, F., Rodríguez, A., Sauvage, L., Schmidt,  
536 J., Schnell, F., Schwarz, A., Seifert, P., Serikov, I., Sicard, M., Silva, A. M., Simeonov, V., Siomos, N., Sirch, T.,  
537 Spinelli, N., Stoyanov, D., Talianu, C., Tesche, M., De Tomasi, F., Trickl, T., Vaughan, G., Volten, H., Wagner,  
538 F., Wandinger, U., Wang, X., Wiegner, M., and Wilson, K. M.: EARLINET all observations (2000–2010),  
539 World Data Center for Climate (WDCC), doi:10.1594/WDCC/EN\_all\_measurements\_2000-2010, 2014a.
- 540 Voss, K. A., Famiglietti, J. S., Lo, M., de Linage, C., Rodell, M. and Swenson, S. C.: Groundwater depletion in  
541 the Middle East from GRACE with implications for transboundary water management in the Tigris-  
542 Euphrates-Western Iran region, *Water Resour. Res.*, 49(2), 904–914, doi:10.1002/wrcr.20078, 2013.
- 543 Vukovic, A., Vujadinovic, M., Pejanovic, G., Andric, J., Kumjian, M. R., Djurdjevic, V., Dacic, M., Prasad, A. K.,  
544 El-Askary, H. M., Paris, B. C., Petkovic, S., Nickovic, S., and Sprigg, W. A.: Numerical simulation of "an  
545 American haboob", *Atmos. Chem. Phys.*, 14, 3211–3230, doi:10.5194/acp-14-3211-2014, 2014.
- 546 Zhang, K. M., Knipping, E. M., Wexler, A. S., Bhave, P. V., and Tonnesen, G. S.: Size distribution of sea-salt  
547 emissions as a function of relative humidity, *Atmos. Environ.*, 39, 3373–3379, 2005.
- 548



549

550

551



552

553 Figure 1. a) Model geopotential height contours (every 10 m) and temperature (color scale in °C) at

554 500mb, 6 September 2015, 00:00 UTC; b) Difference (°C) between model soil temperature and

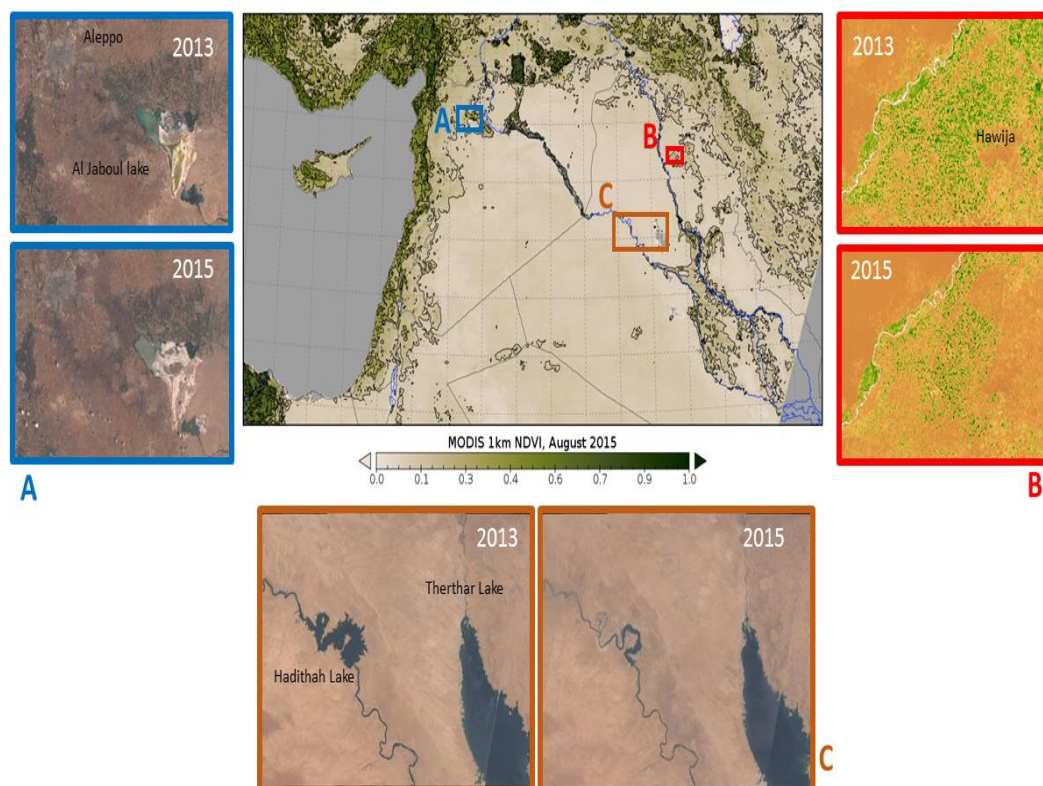
555 model temperature at 2m, 10:00 UTC, 6 September 2015. Black rectangulars indicate the location of

556 the nested model domains (d01:12×12 km, d02:4×4 km, d03:2×2 km).

557



## Land type changes in 2015

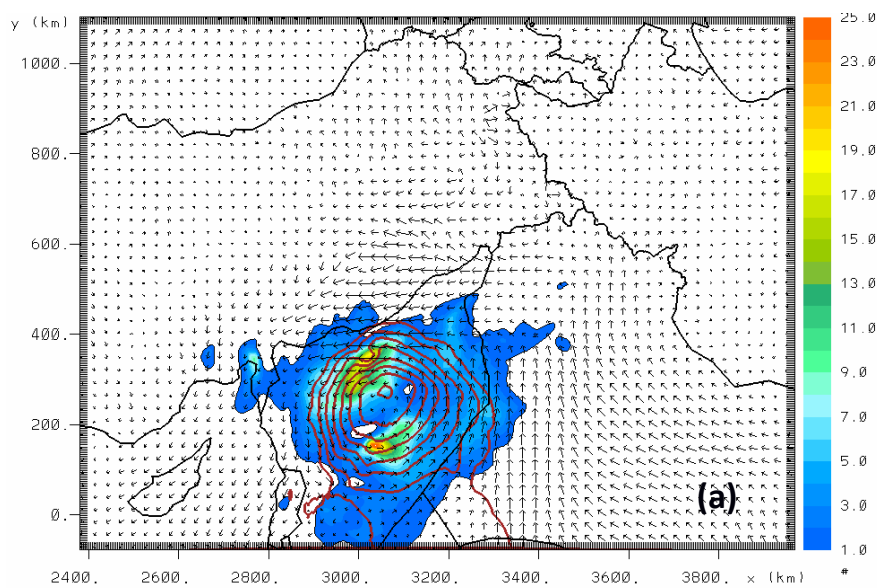


558  
559 Figure 2. (central panel) MODIS NDVI observations for August 2015 were used to identify regions of  
560 bare soil that can be sources of dust aerosols. The contour lines correspond to the major ticks of the  
561 color scale. Large regions of wester Syria and Iraq have NDVI values from 0 to 0.1. The three  
562 subpanels show examples of land type change between summer 2013 and summer 2015. (Subpanel  
563 A) Landsat 8 natural color images of Aleppo region, Syria shows changes of cultivation patterns and  
564 drying of nearby Al Jaboul lake (e.g. the bright areas of the Al Jaboul Lake - dry parts of the lake -  
565 increased from 2013 to 2015); (Subpanel B) Landsat 8 NDVI index images in the region of Hawija,  
566 Kirkuk Province, Iraq reveal that large areas remained uncultivated in 2015 (e.g. the 2013 map  
567 shows many more green spots - agriculturally used areas - than the 2015 map); (Subpanel C)  
568 Landsat 8 natural color images showing diminishing area of Hadithah Lake on the Euphrates river and  
569 the drying up of the Therthar canal and lake.

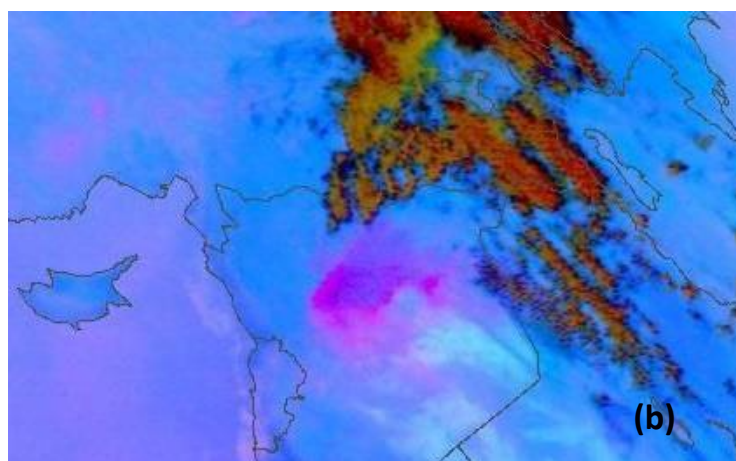
570  
571



572



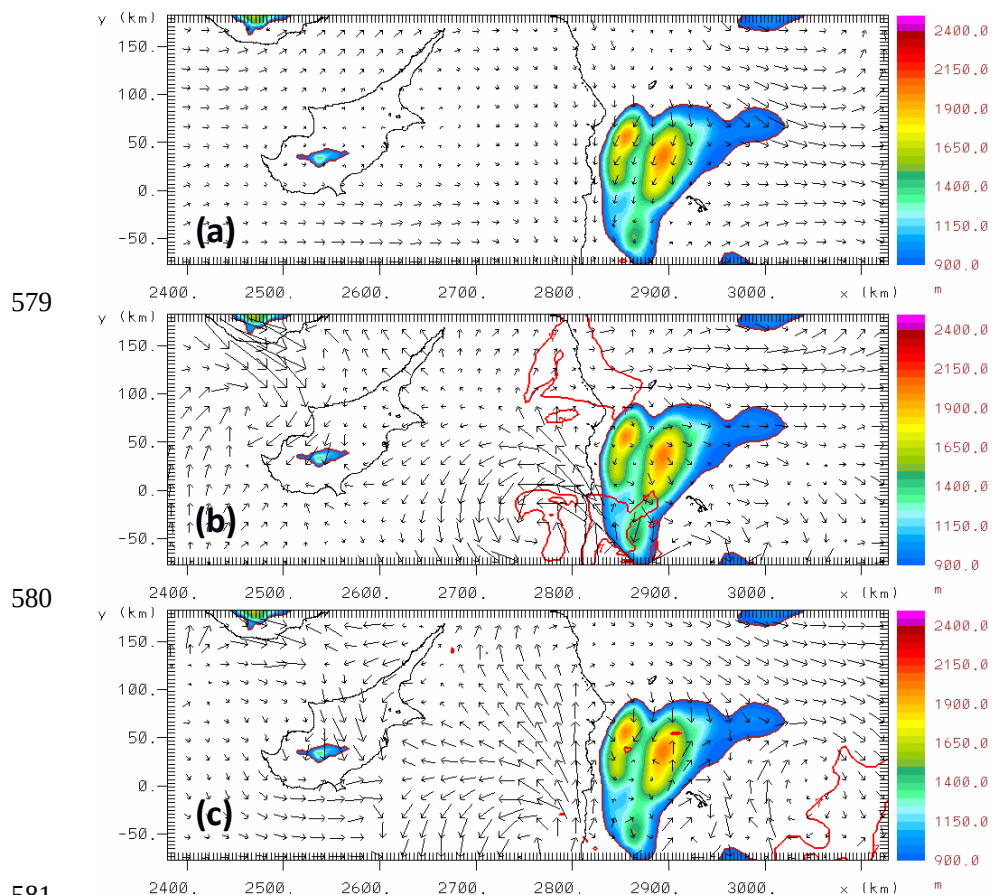
573



574

575 Figure 3. a) Model AOD (color scale) , geopotential height at 850 mb (red contours from 1490 to  
576 1505 m every 2.5 m) and wind vectors at 850mb ; b) MSG SEVIRI dust RGB at 08:00 UTC, 6  
577 September 2015

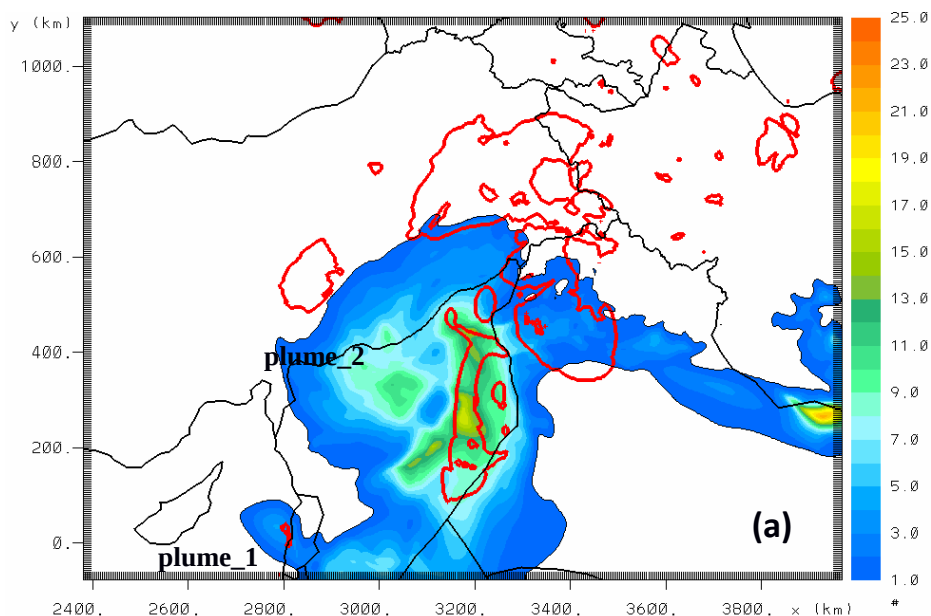
578



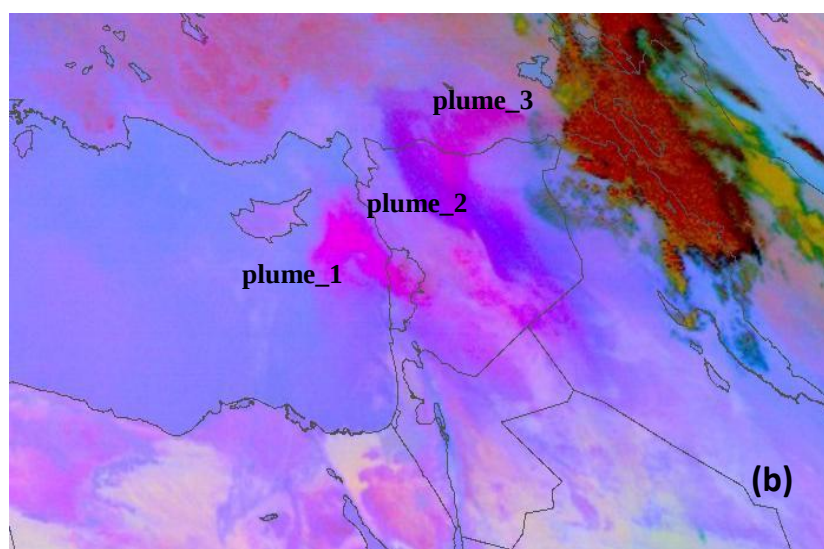
581  
582 Figure 4. Model topography (color scale), wind vectors at the first model layer (50 m) and cloud  
583 fraction > 70% (red contour), zoom from the second model grid, 6 September 2015, 00:00, 06:00,  
584 12:00 UTC.  
585



586  
587



588  
589

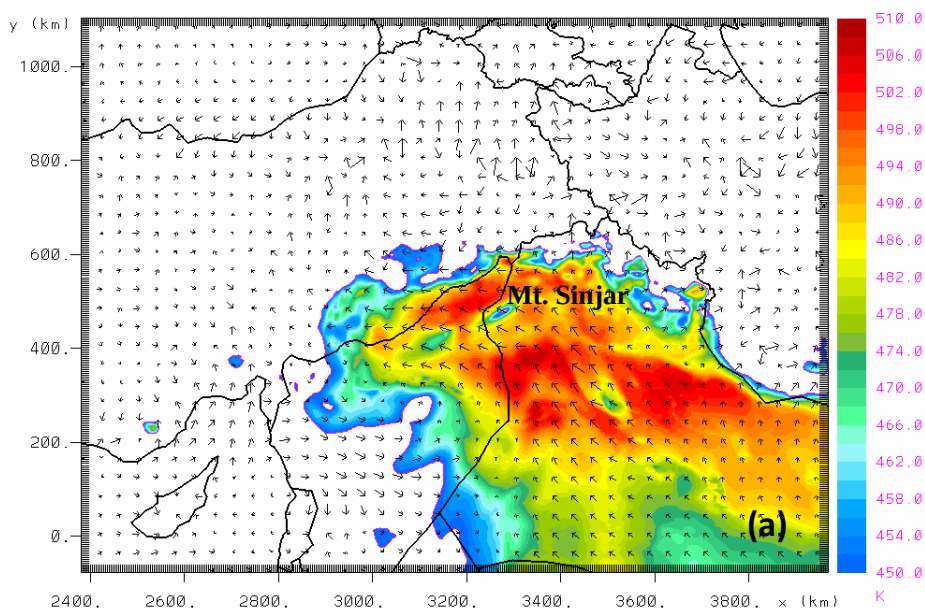


590  
591  
592  
593  
594  
595  
596  
597  
598

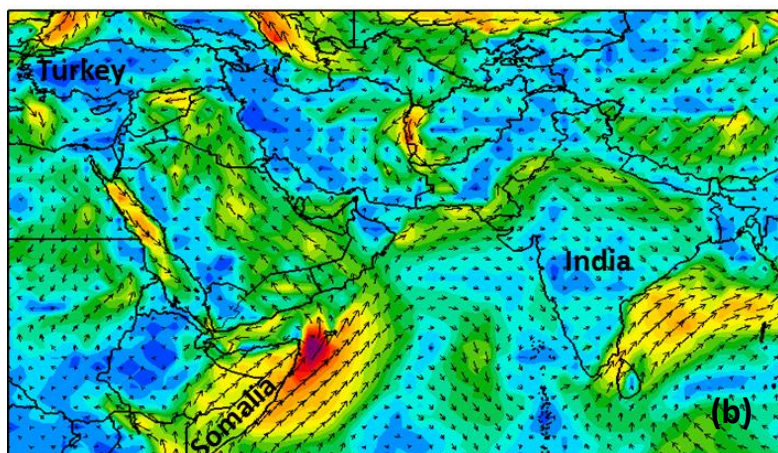
Figure 5. a) Model AOD at 550 nm (color scale) and cloud cover > 70% (red contour). b) MSG-SEVIRI dust RGB component, 7 September 2015, 00:00 UTC



599  
600



601  
602



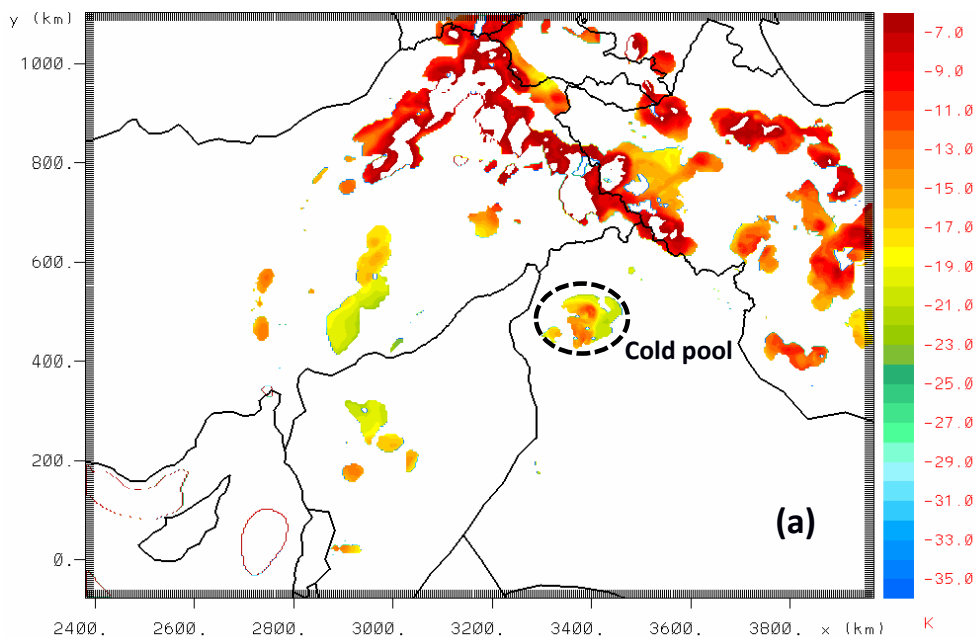
603  
604  
605  
606  
607

Figure 6. a) Model equivalent potential temperature (K) and wind vectors at 50m above ground, 6 September 2015, 13:00 UTC. b) Wind speed at 10m from the NCEP final analysis (FNL) dataset, 6 September 2015, 06:00 UTC.

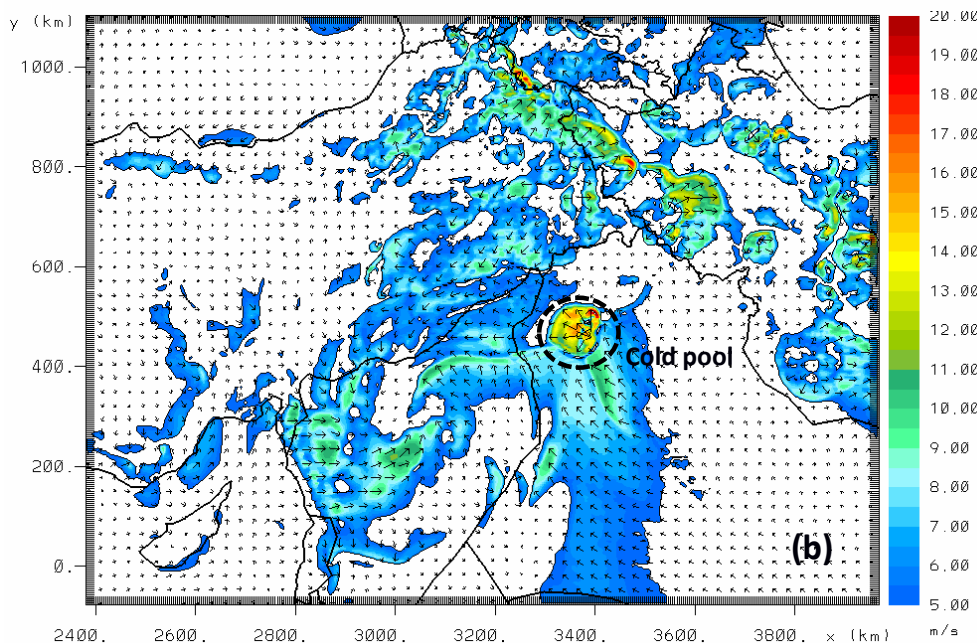




608

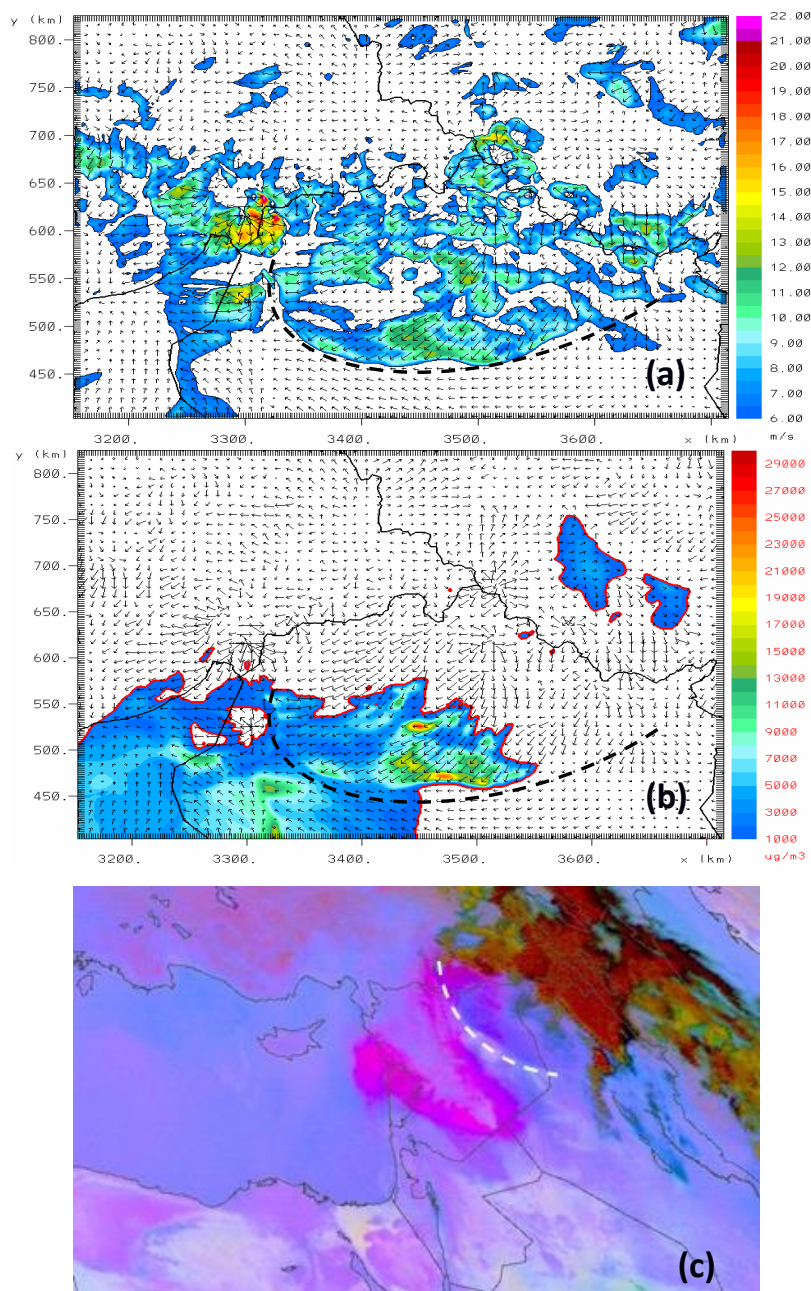


609



610

611 Figure 7. a) Model rain droplets – air temperature difference in K. b) Model wind speed at 10m ( $\text{ms}^{-1}$ ), 6 September 2015, 15:00 UTC. The dashed line denotes the location of the cold pool.  
612



613

614

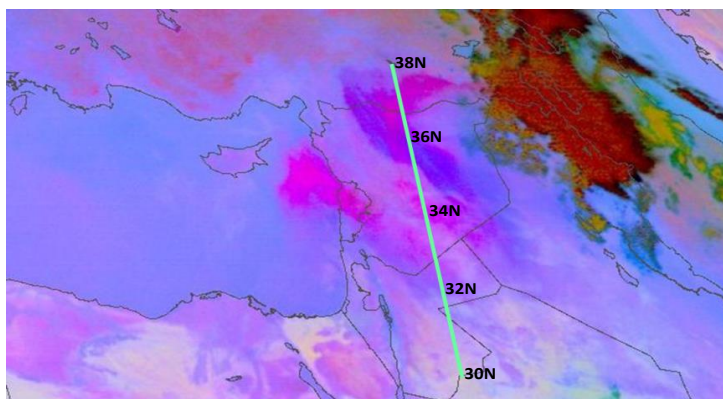
615

616 Figure 8. a) Model wind speed greater that  $6 \text{ ms}^{-1}$  at 10m and b) Near surface model dust  
617 concentration ( $\mu\text{g m}^{-3}$ ) from the inner grid ( $2 \times 2 \text{ km}$ ) c) MSG-SEVIRI RGB component, 6 September  
618 2015, 20:00 UTC. The dashed lines indicates the haboob front location.

619

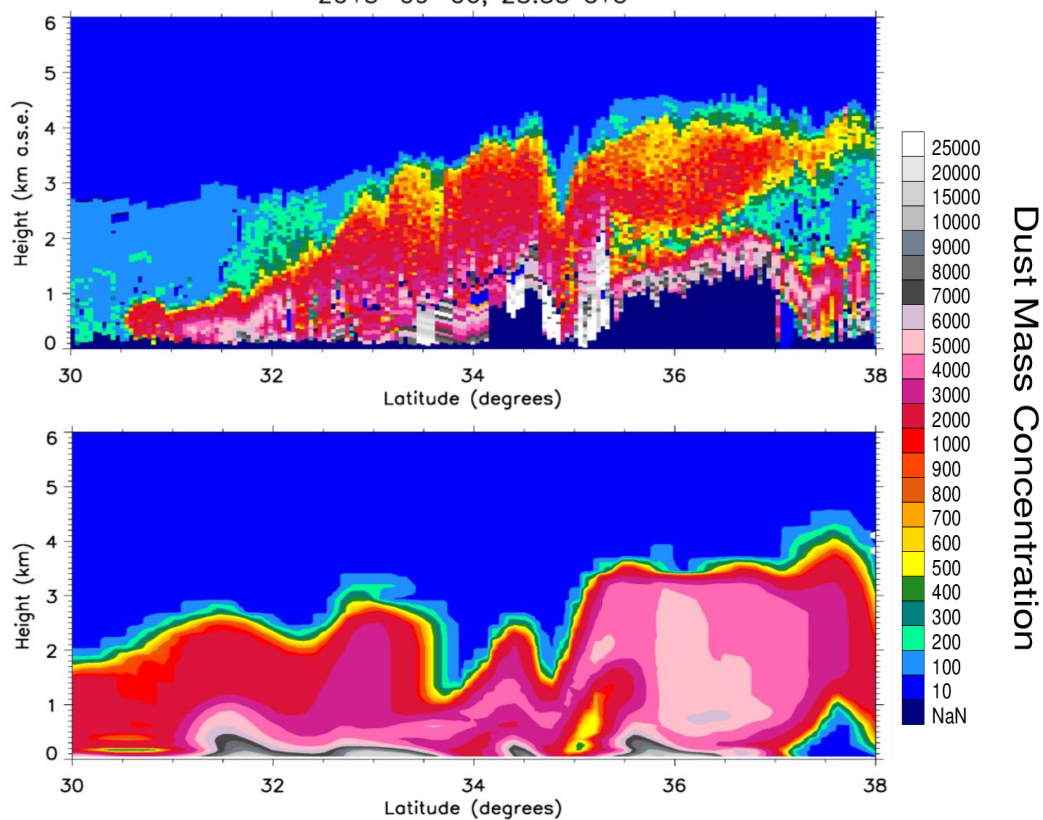


620



621

CALIPSO Dust Mass Concentration ( $\mu\text{g}/\text{m}^3$ )  
2015-09-06, 23:33 UTC



622

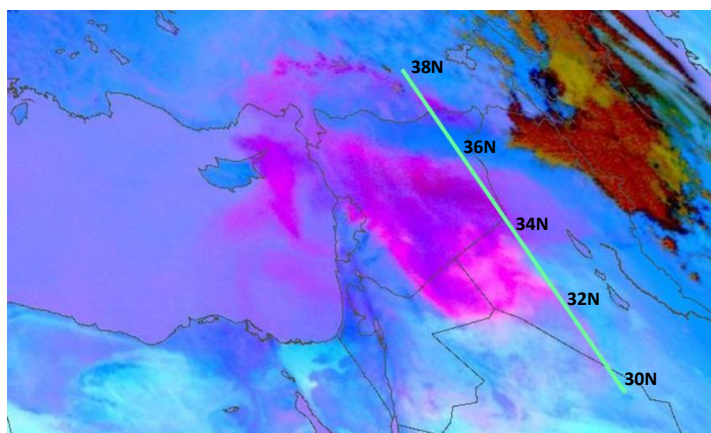
623

624 Figure 9. a) MSG-SEVIRI RGB map and CALIPSO overflight (green line), b) CALIPSO dust mass  
625 concentration ( $\mu\text{g m}^{-3}$ ) and c) model dust mass concentration at 6 September 2015, 23:33 UTC. Due  
626 to the severity of the event CALIPSO signal is totally attenuated below  $\sim 1\text{km}$  a.s.e. in the area  
627 between  $35\text{-}37^\circ\text{N}$  (dark blue color).

628

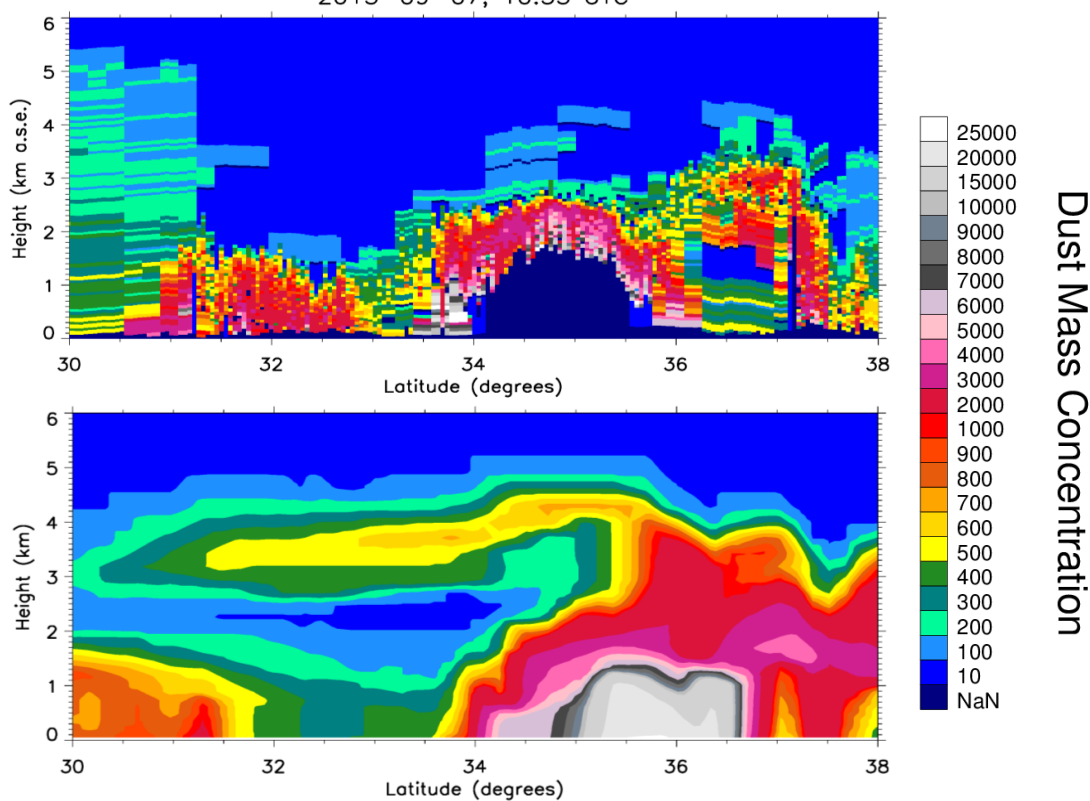


629



630

CALIPSO Dust Mass Concentration ( $\mu\text{g}/\text{m}^3$ )  
2015-09-07, 10:35 UTC



631

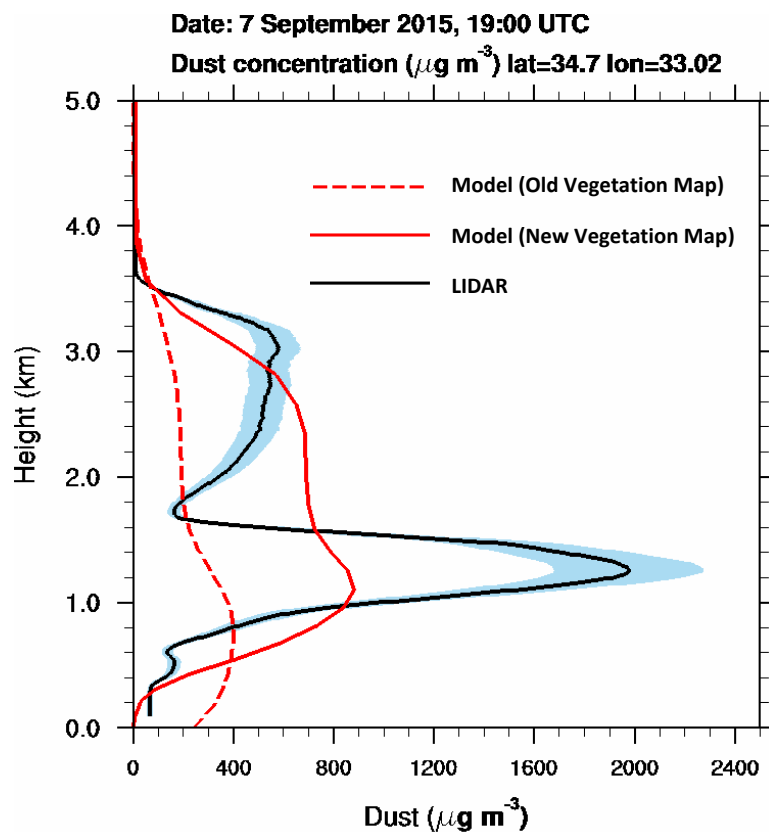
632

633 Figure 10. a) MSG-SEVIRI RGB map and CALIPSO overflight (green line), b) CALIPSO dust mass  
634 concentration ( $\mu\text{g m}^{-3}$ ) and c) model dust mass concentration at 7 September 2015, 10:35 UTC. Due  
635 to the severity of the event CALIPSO signal is totally attenuated bellow  $\sim 1\text{km}$  a.s.e. in the area  
636 between  $34\text{-}36^\circ\text{N}$  (dark blue color).

637



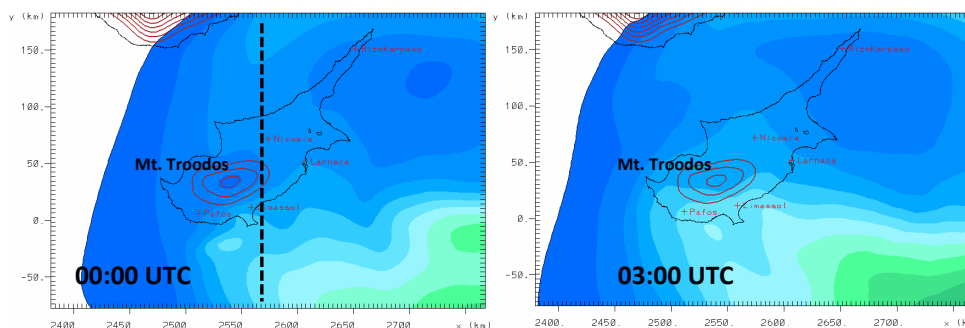
638  
639



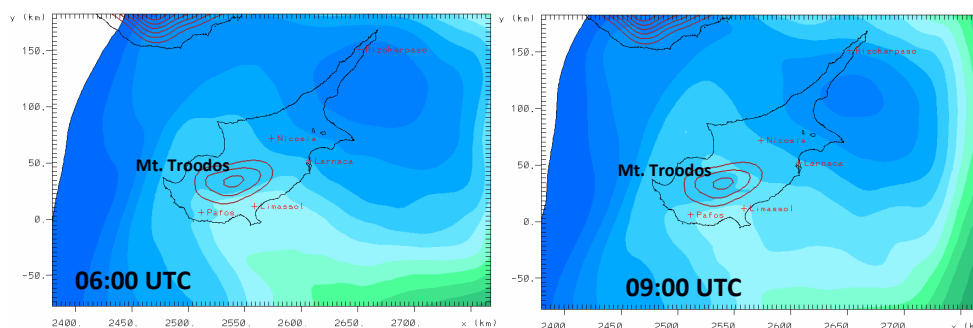
640  
641 Figure 11. Vertical profile of dust concentration on 7 September 19:00 UTC over Limassol. Blue  
642 shadow indicates a 20% uncertainty of the lidar measurements.



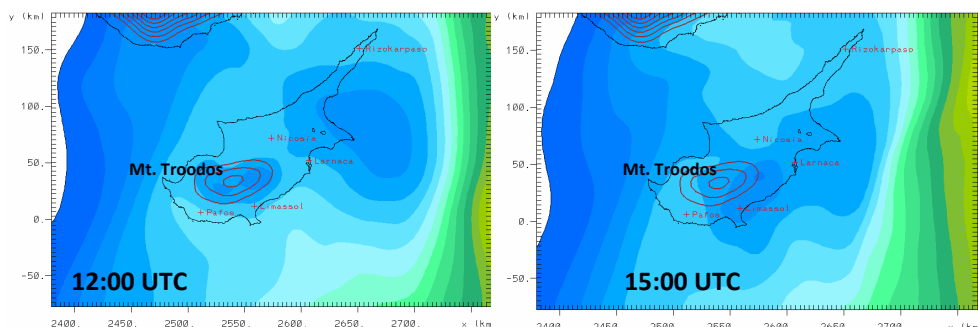
643



644



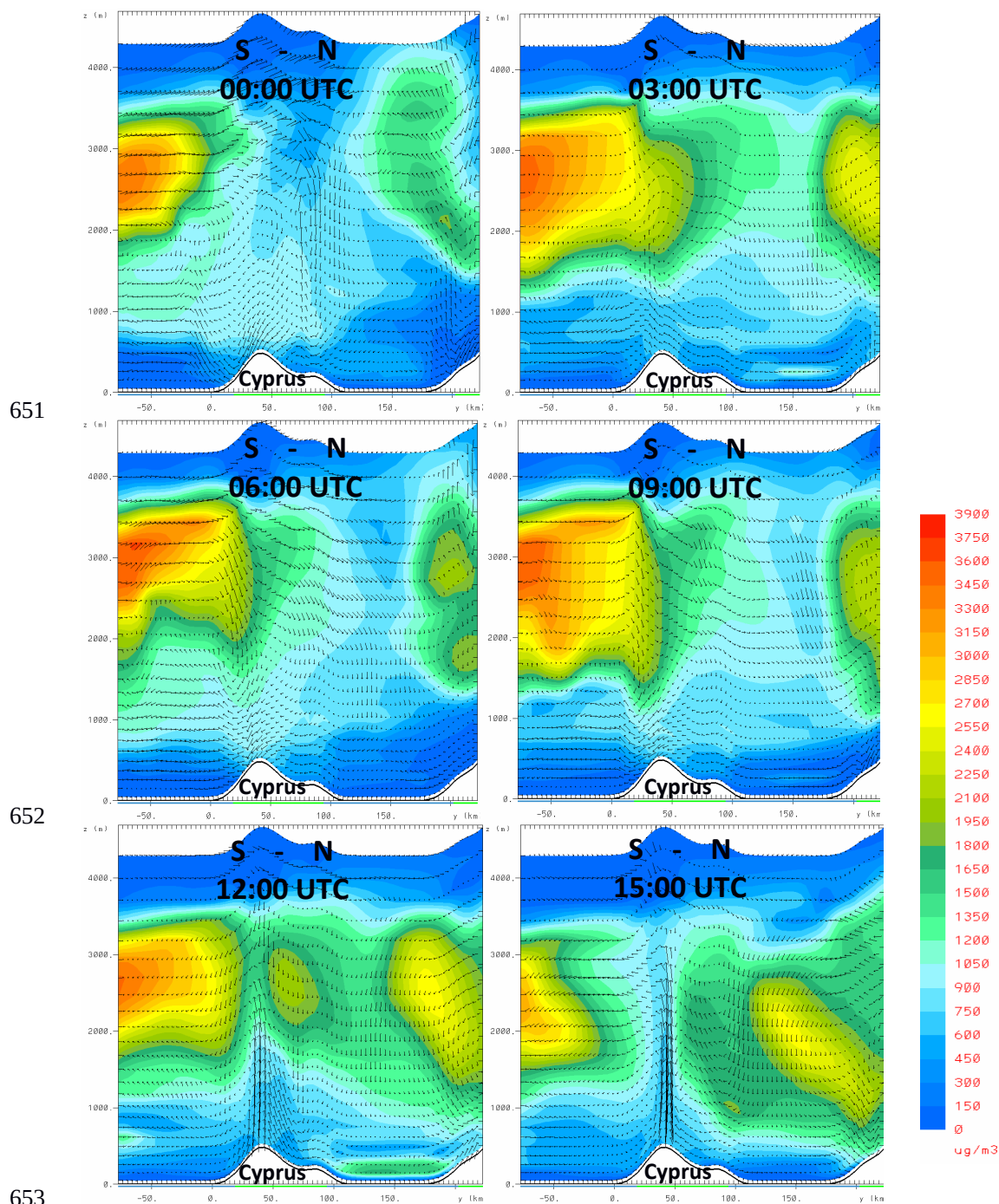
645



646

647 Figure12. Model 550 nm AOT over Cyprus 00:00 – 15:00 UTC, 8 September 2015, zoom from the  
648 second (4×4 km) model domain. The dashed black line shows the location of the cross-sections in  
649 Figure 13.

650



654 Figure 13. Vertical cross-section (South-North) of modeled dust concentration over Cyprus 00:00 –  
655 15:00 UTC, 8 September 2015. The location of the cross-section is shown in Figure 12a.

656